A&A 393, 345–357 (2002)
DOI: 10.1051/0004-6361:20021015
© ESO 2002

Astronomy & Astrophysics

Modelling rapid rotators for stellar interferometry

A. Domiciano de Souza[1], F. Vakili[1,2], S. Jankov[1,3], E. Janot-Pacheco[4], and L. Abe[1]

[1] Observatoire de la Côte d'Azur, Département FRESNEL, CNRS UMR 6528, 2130 route de l'Observatoire, Caussols, 06460 St Vallier de Thiey, France
[2] Département d'Astrophysique de l'Université de Nice/Sophia-Antipolis, CNRS UMR 6525, France
[3] Astronomical Observatory Belgrade, MNTRS 1940, Volgina 7, 11050 Beograd, Yugoslavia
[4] Instituto de Astronomia, Geofísica e Ciências Atmosféricas da Universidade de São Paulo, CP 9638, 01065-970, São Paulo, SP, Brasil

Received 6 March 2002 / Accepted 14 June 2002

Abstract. Optical long baseline interferometry is a powerful tool to study detailed stellar structures. In particular, rapid rotation induces interferometric signatures requiring a detailed modelling for correctly interpreting high angular resolution data. In the present paper we study the effects of uniform stellar rotation on interferometric observables using a physically coherent model that includes gravity darkening and geometrical deformation, as well as a radiation transfer code. We investigate the use of multi-baseline and/or multi-channel observations, both in the continuum and spectral lines, in order to obtain the unique solutions for relevant model parameters. We show that this is possible and we provide a guide for observers in order to perform this task. However, this turns out to be quite demanding in terms of sensitivity requiring the use of new generation interferometers.

Key words. techniques: high angular resolution – techniques: interferometric – techniques: spectroscopic – stars: rotation

1. Introduction

Theory predicts that rotation can deeply impact the structure and evolution of stars. In particular, rapid rotation affects stellar shapes and emitted local flux. Since Optical Long Baseline Interferometry (OLBI) is a technique particularly sensitive to sky projected shapes and brightness distribution, it can contribute to significantly improve our understanding of the rotation effects on stars.

Johnston & Wareing (1970) carried out the first interferometric theoretical study of rotationally distorted stars in the approximation of slow uniform rotation and equator-on stars. They also performed some numerical simulations for Altair and Regulus concluding that observations of rotational distortion was marginally feasible with the early 1970's interferometers. The authors pointed out that the interferometric signature of the apparent stellar oblateness is decreased by the gravity darkening effect foreseen in rapidly rotating stars (von Zeipel 1924).

The first attempt to measure the geometrical deformation of a rapidly rotating star was carried out with the Narrabri intensity interferometer on the bright star Altair (Hanbury Brown 1974). Indeed those observations remained too marginal to critically decide between different models for Altair. Today's operating and near to operating stellar interferometers approach the required accuracies to recover rotational parameters from OLBI data. For instance, Van Belle et al. (2001) observed Altair through OLBI techniques measuring its apparent elongation and establishing constraints upon the relationship between rotation velocity and stellar inclination.

The expected sensitivity of the upcoming generation of stellar interferometers requires refined models adapted to interpret this kind of observation. The development of modern physically coherent numerical models offers nowadays the complete ingredients to build fast and refined numerical tools in order to progress significantly towards the correct interpretation of these high accuracy data, a task that has motivated the present work to prepare future observations with state-of-the-art interferometers.

In Sect. 2 we present an interferometry-oriented model for uniform rapid rotators that includes gravity darkening and geometrical deformation, as well as a radiation transfer code. This model is used in Sect. 3 to evaluate the effects of rapid stellar rotation on the most common interferometric observable, the complex visibility amplitude, in order to identify the optimal observation strategies and the required precisions to constraint the model parameters. In this section we also investigate the uniqueness of the solutions and discuss the obtained results. Finally, in Sect. 4 we present the conclusions of this work.

2. Interferometry-oriented model

In the following we present a rotating star's interferometry-oriented model including solid rotation (Roche approximation), gravity darkening and local plane parallel atmospheres.

Send offprint requests to: A. Domiciano de Souza,
e-mail: Armando.Domiciano@obs-azur.fr

Article published by EDP Sciences and available at http://www.aanda.org or http://dx.doi.org/10.1051/0004-6361:20021015

We first develop the equations defining the stellar shape and the emitted flux, as well as the observable quantities of stellar interferometry. Further, we describe the numerical model used throughout this paper.

2.1. Rotating star's model

We will consider a Roche model for which the following assumptions hold:

(*a*) uniform rotation with angular velocity Ω;
(*b*) all mass M is concentrated in a point at the center of the star.

The stellar equipotential surfaces are then given by:

$$\Psi(\theta) = \frac{\Omega^2 R^2(\theta)\sin^2\theta}{2} + \frac{GM}{R(\theta)} = \frac{GM}{R_\mathrm{p}} \tag{1}$$

where $R(\theta)$ is the stellar radius at colatitude θ, R_p is the polar radius and G is the gravitational constant. We are also assuming that rotation does not affect the polar radius of the star (Collins 1963). In fact there is a slight decrease of R_p with rotation (Collins & Harrington 1966) but that does not alter significantly the results of this work.

Let V_eq be the equatorial linear rotation velocity and R_eq the equatorial radius. Thus, defining the normalized surface radius as:

$$r(\theta) \equiv R(\theta)/R_\mathrm{eq}, \tag{2}$$

the degree of sphericity D of the star as:

$$D \equiv \frac{R_\mathrm{p}}{R_\mathrm{eq}} = 1 - \frac{V_\mathrm{eq}^2 R_\mathrm{p}}{2GM} = \left(1 + \frac{V_\mathrm{eq}^2 R_\mathrm{eq}}{2GM}\right)^{-1} \tag{3}$$

and using the relation $V_\mathrm{eq} = \Omega R_\mathrm{eq}$ we can rewrite Eq. (1) as the following cubic equation:

$$r^3(\theta) - r(\theta)\left(\frac{1}{1-D}\right)\frac{1}{\sin^2\theta} + \left(\frac{D}{1-D}\right)\frac{1}{\sin^2\theta} = 0. \tag{4}$$

Note that the degree of sphericity D is equal to 1 for a spherical star and is less than 1 for a geometrically deformed rotating star. The critical equatorial linear and angular velocities at the equator are given respectively by:

$$V_\mathrm{c}^2 = \frac{GM}{R_\mathrm{c}} = GM\left(\frac{2}{3R_\mathrm{p}}\right) \quad \text{and} \quad \Omega_\mathrm{c} = \frac{V_\mathrm{c}}{R_\mathrm{c}} \tag{5}$$

which implies $D_\mathrm{c} = \frac{2}{3}$. Using Eqs. (3) and (5) the critical rotation ratio is thus:

$$\left(\frac{V_\mathrm{eq}}{V_\mathrm{c}}\right)^2 = 3(1-D) \Rightarrow \left(\frac{\Omega}{\Omega_\mathrm{c}}\right)^2 = 2\frac{(1-D)}{D}\left(\frac{3}{2}D\right)^3. \tag{6}$$

Following Kopal's (1987) notation, the solution of Eq. (4) is written as:

$$r(\theta) = D\frac{\sin\left(\frac{1}{3}\arcsin(\gamma)\right)}{\frac{1}{3}\gamma} = D\ {}_2F_1\left(\tfrac{1}{3},\tfrac{2}{3};\tfrac{3}{2};\gamma^2\right) \tag{7}$$

where ${}_2F_1\left(\frac{1}{3},\frac{2}{3};\frac{3}{2};\gamma^2\right)$ is the hypergeometric series ${}_2F_1$ with an argument given by:

$$\gamma^2 \equiv 2\frac{(1-D)}{D}\left(\frac{3}{2}D\right)^3\sin^2\theta = \left(\frac{\Omega}{\Omega_\mathrm{c}}\sin\theta\right)^2. \tag{8}$$

The modulus of local effective surface gravity $g = |\boldsymbol{\nabla}\Psi|$ is given by:

$$g(\theta) = \frac{GM}{R_\mathrm{p}^2}D^2\left(\frac{2}{3D}\right)^3\left\{\left[r(\theta)\left(\frac{\Omega}{\Omega_\mathrm{c}}\right)^2\sin\theta\cos\theta\right]^2 + \left[\frac{1}{r^2(\theta)}\left(\frac{3}{2}D\right)^3 - r(\theta)\left(\frac{\Omega}{\Omega_\mathrm{c}}\sin\theta\right)^2\right]^2\right\}^{1/2}. \tag{9}$$

Equation (9) is written in the form $g(\theta) = g_\mathrm{p}\, g_\mathrm{n}(\theta)$, where $g_\mathrm{p}\left(= GMR_\mathrm{p}^{-2}\right)$ is the polar gravity and $g_\mathrm{n}(\theta)$ is the effective surface gravity normalized by the polar one. Note that, by considering Eqs. (6), (7) and (8), $g_\mathrm{n}(\theta)$ is totally defined by the degree of sphericity D and the colatitude θ. Equation (9) is written in a similar form as given by Collins (1965), but with the radius $R(\theta)$ normalized by R_eq instead of R_p (Eq. (2)).

In order to complete the description of the physical model we consider that the stellar atmosphere may be approximated locally by a plane parallel model with adequate effective temperature ($T_\mathrm{eff}(\theta)$) and gravity ($g(\theta)$). We remind that $T_\mathrm{eff}(\theta)$ is related to the local stellar radiative flux $F(\theta)$ by $F(\theta) = \sigma T_\mathrm{eff}^4(\theta)$, where σ is the Stefan-Boltzmann constant. For rotating stars von Zeipel's (1924) theorem says that the local flux is proportional to g, or alternatively, $T_\mathrm{eff} \propto g^{0.25}$. This expression for the gravity darkening is strictly valid only for conservative rotation laws (centrifugal force derivable from a potential) and radiative flux in the diffusion approximation. For stars with convective envelopes, Lucy (1967) showed that $T_\mathrm{eff} \propto g^{0.08}$. More generally, conservative rotation laws result in $T_\mathrm{eff} \propto g^\beta$ where the value of β depends on the different approximations chosen for the radiative transfer, opacity laws, model atmospheres, etc. The local effective temperature can thus be written as:

$$T_\mathrm{eff}(\theta) = T_\mathrm{p}\left(\frac{g(\theta)}{g_\mathrm{p}}\right)^\beta = T_\mathrm{p}\, g_\mathrm{n}^\beta(\theta) \tag{10}$$

where T_p is the polar effective temperature.

Claret (1998) tabulated values of β for a wide range of stellar models achieving a smooth transition between convective and radiative energy transport mechanisms in stellar envelopes. Pérez Hernández et al. (1999) applied a general law of the form of Eq. (10) for A and F type stars where β has been considered constant for a given rotating star. However, the validity of Eq. (10) remains questionable when the effects of differential rotation are taken into account (Connon Smith & Worley 1974). They showed that in this case no singular value of β describes a physical stellar surface and that β exceeds the von Zeipel value of 0.25. Claret (2000) gives an analytical expression for the latitude dependence of β as a function of relevant stellar parameters, notably, the atmospherical and internal structure parameters and the adopted rotation law.

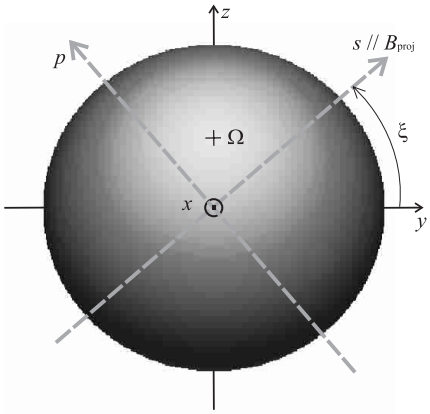

Fig. 1. Adopted reference system for a rotating star. The cross indicates the point where the rotation axis crosses the stellar surface. This rotation axis forms an angle i (not represented in the figure) with the observer's direction (x axis) and its projection onto the sky is parallel to the z axis. The sky projected interferometer baseline $\boldsymbol{B}_{\mathbf{proj}}$ forms an angle ξ with the y axis and defines a new sky projected coordinate system (s, p) for which the s direction is parallel to $\boldsymbol{B}_{\mathbf{proj}}$.

In this paper we treat the stars for which Eq. (10) is valid, e.g., without differential rotation. The effects of differential rotation on the shape of absorption lines has been discussed by Reiners & Schmitt (2002) who gave a simple procedure for the determination of differential rotation from the first two zero positions of the line profile's Fourier transform. The case of deformed differentially rotating stars from the interferometrical point of view will be considered in a forthcoming paper.

2.2. Interferometric observables

Interferometers measure fringe contrasts and positions which correspond, respectively, to the amplitudes and phases of the *complex degree of coherence* or, alternatively, the *complex visibility*. For a given sky-projected monochromatic brightness distribution I_λ (also called intensity map), the Van Cittert-Zernike theorem (Born & Wolf 1980) allows us to relate the observed complex visibilities V to the Fourier transform of I_λ normalized by its value at the origin, i.e.,

$$V(f_y, f_z, \lambda) = \left|V(f_y, f_z, \lambda)\right| \mathrm{e}^{\mathrm{i}\phi(f_y, f_z, \lambda)} = \frac{\widetilde{I}_\lambda(f_y, f_z)}{\widetilde{I}_\lambda(0,0)} \tag{11}$$

where $\widetilde{I}_\lambda$ is given by:

$$\widetilde{I}_\lambda(f_y, f_z) = \iint\limits_{S_{\mathrm{vis}}} I_\lambda(y, z) \mathrm{e}^{-\mathrm{i}2\pi(y f_y + z f_z)} \mathrm{d}y \mathrm{d}z. \tag{12}$$

The integration domain is defined by the visible object's surface S_{vis}. The Fourier spatial frequencies f_y and f_z are associated with the coordinates y and z which represent, for example, the right ascension and declination. However, within the framework of this paper it is more convenient to relate them to a coordinate system where the star's projected rotation axis coincides with the z axis (Fig. 1).

OLBI normally works with diluted apertures (separate telescopes or masked mirrors) where each pair of apertures defines a vector baseline projected onto the sky $\boldsymbol{B}_{\mathbf{proj}}$ which forms a baseline position angle ξ with the y axis so that:

$$\boldsymbol{B}_{\mathbf{proj}} = \left(B_{\mathrm{proj}} \cos\xi\right) \hat{y} + \left(B_{\mathrm{proj}} \sin\xi\right) \hat{z} \tag{13}$$

where $\hat{y}$ and $\hat{z}$ are unit vectors (Fig. 1). Each sky-projected baseline defines a new coordinate system (s, p) in the tangent plane which is related to (y, z) by:

$$\begin{aligned} s &= y\cos\xi + z\sin\xi \\ p &= -y\sin\xi + z\cos\xi. \end{aligned} \tag{14}$$

In the (s, p) coordinate system $\boldsymbol{B}_{\mathbf{proj}}$ is parallel to the s direction, represented by the unit vector $\hat{s}$. Observations at each baseline contain high angular resolution information at spatial frequencies given by $\boldsymbol{B}_{\mathbf{proj}}\, \lambda_{\mathrm{eff}}^{-1}$, where λ_{eff} is the effective wavelength of the spectral band considered; its value depends on the spectral response of the instrument. We can thus define the new spatial frequency coordinates (u, v) for which $\boldsymbol{B}_{\mathbf{proj}}\, \lambda_{\mathrm{eff}}^{-1}$ is parallel to the unit vector $\hat{u}$. The (u, v) coordinates are related to (f_y, f_z) by a transformation analogous to Eqs. (14).

In the approximation of small apertures compared to $\left|\boldsymbol{B}_{\mathbf{proj}}\right|$ it is simpler to consider linear cuts along the Fourier plane corresponding to a given baseline direction $(\hat{s})$. In that case Eq. (12) can be rewritten as:

$$\widetilde{I}_{\lambda,\xi}(u) = \int I_{\lambda,\xi}(s) \mathrm{e}^{-\mathrm{i}2\pi s u} \mathrm{d}s \tag{15}$$

where $I_{\lambda,\xi}(s)$ is the line integral of $I_\lambda(s, p)$ over p for a given ξ. Note that v does not appear in Eq. (15). Analogously to Eq. (11) the *line complex visibility* is given by:

$$V_\xi(u, \lambda) = \left|V_\xi(u, \lambda)\right| \mathrm{e}^{\mathrm{i}\phi_\xi(u,\lambda)} = \frac{\widetilde{I}_{\lambda,\xi}(u)}{\widetilde{I}_{\lambda,\xi}(0)}. \tag{16}$$

Equations (15) and (16) say that the interferometric information along $\boldsymbol{B}_{\mathbf{proj}}$ is identical to the one dimensional Fourier transform of the curve resulting from an integration of the brightness distribution in the direction perpendicular $(\hat{p})$ to this baseline. Bracewell (1956) presents a much deeper discussion on the advantages in using strip and line (the limiting case of zero strip width) integrations when interpreting interferometric observations.

Since stellar interferometry is sensitive to sky projected angular sizes it allows a scaling of theoretical models which can be matched to interferometric data. Thus, for a given star one can estimate the linear radius through the distance d which is provided by precise Hipparcos (Perryman et al. 1997) measurements for nearby stars.

The presented model is thus defined by five parameters which describe the star intrinsically, such as: R_{p}, T_{p}, g_{p}, D and β. In addition to those there are two non-intrinsic parameters: the stellar inclination i and the sky projected baseline position angle ξ. Examples of variations of apparent temperature distribution and geometrical deformation with respect to inclination are given in Fig. 2. Remember that ξ gives information on the direction of the sky projected rotation axis which is important for example for comparisons between OLBI and polarimetric observations. Finally, $I_\lambda(y, z)$ is also dependent on the adopted model atmosphere and spectral coverage.

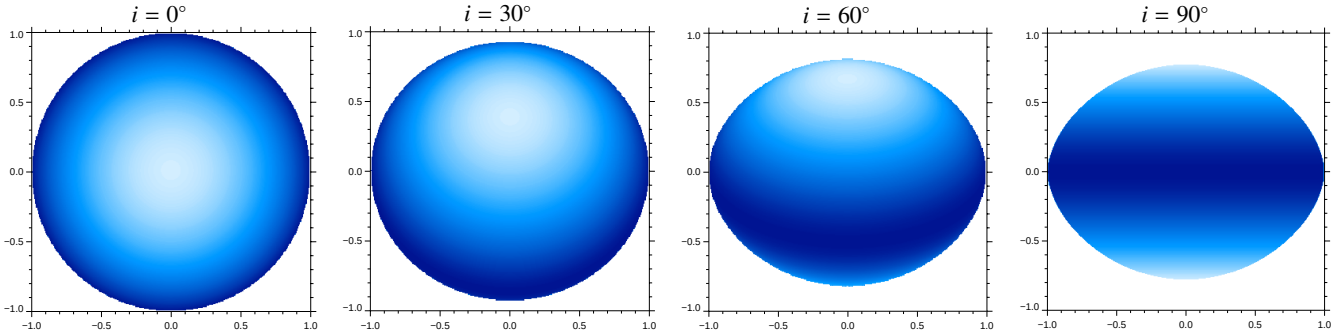

Fig. 2. Effective temperature maps for $D = 0.78$ (model A in Table 1), $\beta = 0.25$ and different inclinations. The polar (maximum) and equatorial (minimum) effective temperatures are $T_p = 35\,000$ K and $T_{eq} = 25\,100$ K, respectively. Abscissas (y) and ordinates (z) are normalized by the equatorial radius R_{eq}. Note that the projected geometrical deformation increases with higher inclinations but the stellar size in the y direction is constant. Since the local radiative surface flux is defined by $F(\theta) = \sigma T_{eff}^4(\theta)$ this figure gives and idea of the projected brightness changes from pole to equator.

2.3. Numerical model

Since the intensity maps are projections of the 3D stellar surface onto the sky (yz plane) a non-equally spaced projected stellar grid is used in the adopted numerical model. We thus developed a Fourier transform algorithm adapted to unequally spaced points to evaluate the complex visibilities, avoiding any interpolation on the discrete intensity maps which would result in more time consuming calculations and losses in numerical precision.

A discrete form of the Eq. (12) is obtained by replacing the double integral by a summation on the visible grid points with coordinates y_j and z_j. The index j ranges from 1 to the number of visible grid points N. In addition, the projected visible surface of the grid $S_{vis,j}$ is introduced as a weighting parameter that prevents aliasing due to the unequally spaced points distribution. The discrete Fourier transform of the sky-projected monochromatic brightness distribution is then computed as:

$$\widetilde{I}_\lambda(f_{y,k}, f_{z,l}) = \sum_{j=1}^{N} I_\lambda(y_j, z_j) e^{-i2\pi(y_j f_{y,k} + z_j f_{z,l})} S_{vis,j} \qquad (17)$$

where $f_{y,k}$ and $f_{z,l}$ are the discrete spatial frequency points. The integrations are carried out for equally spaced points in the Fourier plane, so that the trigonometric functions can be evaluated as a combination of summations and multiplications of the step and initial frequency points (Kurtz 1985). This procedure is less time consuming than a classical Discrete Fourier Transform which calculates explicitly the trigonometric functions for each spatial frequency point.

An additional gain in calculation time is obtained because we can calculate specific regions in the Fourier space with any desired sampling. This is generally not possible with the standard Fast Fourier Transform algorithms for which we are constrained to calculate large images in order to obtain an acceptable sampling.

In order to evaluate the intensity maps I_λ figuring in Eq. (17) we used the code BRUCE (Townsend 1997) which creates a stellar grid with local values of effective temperature, gravity, velocity field, projected surface and surface normal direction. In the next step of the modelling process the codes TLUSTY and SYNSPEC (Hubeny 1988; Hubeny & Lanz 1995) are used to generate a grid of synthetic local specific intensities for different values of effective temperature (T_{eff}), gravity (g), chemical abundance, microturbulent velocity (V_{turb}) and cosine of the angle between the the local surface normal and the observer (μ). Throughout this paper specific intensity grids were calculated for solar metallicity, $V_{turb} = 3$ km s^{-1}, and steps in T_{eff}, $\log g$ and μ of 500 K, 0.1 dex and 0.05, respectively. At each stellar grid point a quadrilinear interpolation on the synthetic spectra is applied in order to build discrete intensity maps for each wavelength bin.

The results presented in Sect. 3 are based on stellar models with parameters for the polar regions (R_p, T_p and g_p) corresponding to a spectral type around B0V (Table 1). The remaining free parameters (D, β, i and ξ) are in fact the parameters most closely related to the stellar characteristics for which the OLBI is more sensitive, i.e., the non uniform projected brightness distribution and the geometrical deformation.

Table 1. Some relevant parameters for the two adopted rotation models which correspond to a highly ($D = 0.78$) and a medium ($D = 0.88$) deformed early type star. The adopted polar parameters are $R_p = 6\,R_\odot$, $T_p = 35\,000$ K and $\log g_p = 4.085$ dex ($\Rightarrow M = 16\,M_\odot$).

Model	D	R_{eq} ($R_\odot$)	V_{eq} (km s^{-1})	$\frac{V_{eq}}{V_c}$	$\log g_{eq}$ (dex)	T_{eq}^a (K)
A	0.78	7.694	473.13	0.81	3.508	25 103
B	0.88	6.819	349.43	0.60	3.836	30 314

[a] for $\beta = 0.25$.

Two stellar rotation scenarios were chosen corresponding to rapid and intermediate rotation rates: $V_{eq} \simeq 80\% V_c$ ($\Rightarrow D = 0.78$) and $V_{eq} \simeq 60\% V_c$ ($\Rightarrow D = 0.88$). Consistent with the adopted polar parameters, calculations were performed for gravity darkening coefficients corresponding to early type stars ($\beta = 0.25$). Effective temperature maps for model A in Table 1 ($D = 0.78$) with $\beta = 0.25$ are shown by Fig. 2 for different inclinations.

Although not theoretically predicted for hot stars, the case $\beta = 0$ is also considered in this paper to better distinguish the individual effects of gravity darkening and geometrical

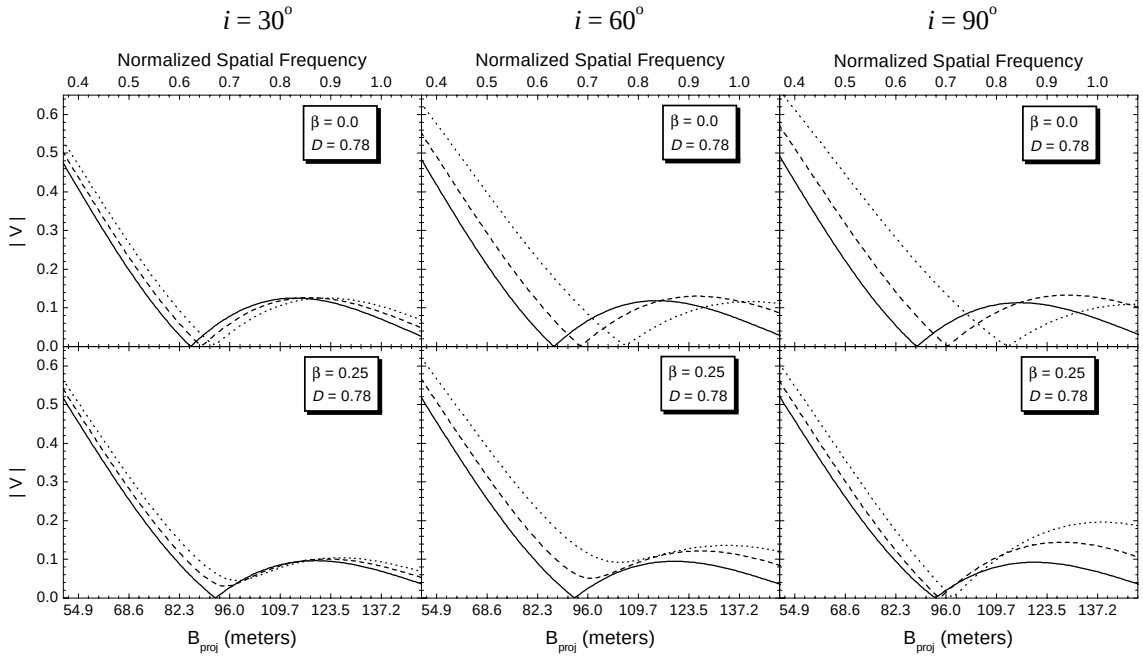

Fig. 3. Complex visibility amplitudes $|V|$ as a function of $B_{\rm proj}$ (in meters) for model A (Table 1) at selected values of ξ, i and β. An angular equatorial radius ($\rho_{\rm eq}$) of 1 milliarcsec was adopted for the plots. Calculations were performed inside a narrow spectral band centered on the blue adjacent continuum corresponding to HeI6678 ($\lambda_{\rm eff}$ = 6654 Å). Part of the first and the second $|V|$ lobes are shown. The curves cover part of the first and the second $|V|$ lobes for three different projected baseline orientations corresponding to $\xi = 0°$ (solid), 45° (dashes) and 90° (dots). The abscissa scale at the top of the figure is presented in normalized spatial frequencies defined by $\rho_{\rm eq} \boldsymbol{B}_{\rm proj}\, \lambda_{\rm eff}^{-1}$.

deformation. By comparing the results for $\beta = 0.25$ and $\beta = 0$ one can easily see the importance of including a correct gravity darkening law in the model. Moreover, the $\beta = 0$ model gives insight into stars with convective envelopes for which low β values are predicted (Lucy 1967).

Both two (Eq. (11)) and one (Eq. (16)) dimension complex visibilities can be calculated by this model but in the present work only the line complex visibility amplitude $|V_\xi(u, \lambda)|$ (hereafter represented as $|V|$) is considered.

3. Observation strategies for determination of model parameters

The results presented here are divided in the domains of monochromatic (or single spectral band) and polychromatic (or multiple spectral bands) OLBI observations.

3.1. Single spectral band OLBI

3.1.1. Interferometric signature of rapid rotation

Figure 3 shows several $|V|$ curves in the vicinity of the first minima and second maxima. Calculations were carried out for model A (Table 1) with different combinations of ξ, i and β inside a narrow spectral band centered on a continuum region close to the photospheric line HeI6678 ($\lambda_{\rm eff}$ = 6654 Å). The curves are given as a function of the sky projected baseline $B_{\rm proj}$ (in meters) for an adopted angular equatorial radius $\rho_{\rm eq}$ of 1 milliarcsec. These are realistic values for bright early type stars and for the available baselines of present and near future interferometers. For a better comparison with the results from the next sections the abscissa scale at the top of Fig. 3 is presented in *normalized spatial frequencies* (u) defined by $\rho_{\rm eq} \boldsymbol{B}_{\rm proj}\, \lambda_{\rm eff}^{-1}$.

Note that in general ξ needs to vary between 0° and 180° for a non pole on star to be completely covered. Since we consider the visibility amplitudes $|V|$ the results will be presented for ξ between 0° to 90° because in this case identical $|V|$ curves are obtained for ξ and $(180° - \xi)$.

For $\beta = 0$ only limb darkening and the geometrical effects due to the Roche model are present. In that case the upper row of Fig. 3 shows that the value of $|V|$ at a given spatial frequency is highly dependent on ξ while the curves have roughly the same form. On the other hand, important changes in the $|V|$ curves occur when gravity darkening is included ($\beta = 0.25$). For high inclinations ($i \geq 60°$) the differences in $|V|$ for a given spatial frequency within the first lobe become much weaker than before and the heights of the second lobes and of the first minima become very dependent on i and ξ. For low i the second maxima are smaller than for the case $\beta = 0$.

The results from Fig. 3 can be qualitatively understood with the help of Eqs. (15) and (16). For $\beta = 0$ one has simply a one dimensional Fourier transform of a centrally symmetric (even) curve, similar to that of a spherical limb darkened star, but with a different angular diameter depending on the baseline position angle. As a result the first minima positions of $|V|$ are just shifted and the height of the second maxima of $|V|$ is almost constant, with the exact value depending on the limb darkening strength.

However, when gravity darkening is included its additional brightness distribution has important consequences on the line

integral $I_{\lambda,\xi}(s)$, resulting in three main configurations depending on i and ξ:

(*a*) *nearly pole-on stars or* $\xi \cong 0°$: almost centrally symmetric $I_{\lambda,\xi}(s)$ that mimics a star with a strong limb darkening, shifting the first minima positions to higher spatial frequencies and lowering the secondary maxima;
(*b*) *nearly equator-on stars and high* ξ *values*: almost centrally symmetric $I_{\lambda,\xi}(s)$ that mimics a limb brightened star shifting the first minima positions to smaller spatial frequencies and increasing the secondary maxima;
(*c*) $i \neq 0°$, $90°$ *and* $\xi \neq 0°$: not centrally symmetric $I_{\lambda,\xi}(s)$ resulting in first minima different from zero.

From Fig. 3 it is thus clear that $|V|$ sensitive to the relevant parameters of the rapid stellar rotation model, particularly when one has access to a large range of baseline projections (separation and position angle). By comparing different curves we note that the rapid rotation signatures can attain amplitudes of several percents which is strong enough to be detected by present and near future interferometers. Thus, the optimal observation strategy would consist of observing the star continuously in a $90°$ range of of ξ. If the projected stellar polar axis orientation is not known a priori one needs to observe in a $180°$ range of baseline orientations in order to ascertain the previous condition. Even in that case, for realistic observations only a limited number of baselines are available, leading, in general, to solutions which are degenerate due to the relatively high number of relevant unknowns of the model, as will be shown in the following.

3.1.2. The uniqueness problem

In interferometric observations one has access to a discrete set of $|V|$ and its associated uncertainties for the corresponding values of $\boldsymbol{B}_{\mathbf{proj}}\,\lambda_{\mathrm{eff}}^{-1}$. Ultimately, one would like to translate these observations in terms of model parameters and their corresponding uncertainties. This can be performed by minimizing a given functional including the data points, the relevant model parameters and constraints on the solutions. A practical application of this kind of multi-parametric search on interferometric data of rapid rotators is presented by van Belle et al. (2001). They adopted a uniform rotating model without gravity darkening and even in this case the uniqueness problem was the major difficulty during the data analysis. This should be our case as well, since we adopt a more general analysis by introducing the parameter β which increases the dimension of the solution space. In fact, degenerate solutions are expected to appear specially when (1) the observations were not carried out on regions of high sensitivity on the model parameters, even for small error bars and/or when (2) the model is too complex for the available error bars.

In order to allow better visualization of the non uniqueness problem we reduce the parameter space by normalizing the spatial frequency by the angular equatorial radius ρ_{eq}. Consequently, in the following analysis the results are presented as a function of normalized spatial frequencies (u) given by $\rho_{\mathrm{eq}}\boldsymbol{B}_{\mathbf{proj}}\,\lambda_{\mathrm{eff}}^{-1}$. Since the angular equatorial radius is, in general, a free variable, its associated measurement errors $\sigma\rho_{\mathrm{eq}}$ should be considered in our analysis to simultaneously determine the complete set of parameters. These errors will influence the determination of the normalized spatial frequencies producing a corresponding uncertainty in $|V|$ at a given frequency. Since the normalized spatial frequencies scale with ρ_{eq} we estimated the influence of $\sigma\rho_{\mathrm{eq}}$ on $|V|$ from the numerical derivative of the $|V|$ curves. Inside the first lobe a good analytical approximation for the visibility uncertainties σV due to $\sigma\rho_{\mathrm{eq}}$ is given by (Vakili et al. 1997):

$$\frac{\sigma\rho_{\mathrm{eq}}}{\rho_{\mathrm{eq}}} = \frac{\sigma V}{|2J_2(z)|} \tag{18}$$

where J_2 is the Bessel function of the first kind and second order.

An instructive way to investigate $|V|$ inside the first lobe is shown by Fig. 4 for selected values of i, β, D, and for the extreme values of ξ ($0°$ and $90°$). Note that $|V|$ is sensitive to these parameters and, in particular, for fixed i and D, the curves of extreme ξ are closer to each other for $\beta = 0.25$ than for $\beta = 0$ at high inclinations ($i \geq 60°$). The presence of gravity darkening induces a partial cancellation of the rotational deformation's signature in the first $|V|$ lobe. For low inclinations (Fig. 4 bottom) this cancellation effect is negligible but the $|V|$ curves for $\beta = 0.25$ are displaced upwards because the star resembles a strong limb-darkened one.

From Fig. 4 one can easily interpolate or extrapolate the behavior of the $|V|$ curves for β values other than 0 and 0.25. In particular, in the frame of our uniform rotation model, for $\beta > 0.25$ the cancellation of the geometrical deformation's signature would be even stronger for high inclinations.

The uncertainties in $|V|$ due to a 1% error in ρ_{eq} are represented as vertical error bars in Fig. 4 for normalized spatial frequencies equal to 0.4. Precisions at the 1% level in stellar diameters/radii are attained by current interferometers. The error bars σV are shown for the higher and lower $|V|$ curves so that one can estimate the intermediate ones from these two extreme values. The choice of $u = 0.4$ corresponds to $|V|$ around 0.5 which is a contrast level relatively easy to measure.

Although the error bars shown in Fig. 4 represent just the influence of errors in ρ_{eq}, they are also an indication of the acceptable observational uncertainties for the rotational signatures to be detected. For observational uncertainties in $|V|$ of the order of values shown in Fig. 4 the dependence of $|V|$ with β would be difficult to assess and for higher uncertainties even the difference between the $|V|$ curves at the extreme values of ξ might not be detected. Clearly, low i (bottom row) and/or low D (right column) are the most demanding in terms of observational precision.

The dependence of $|V|$ with ξ is detailed in Fig. 5 (top rows for fixed i) for the normalized spatial frequency $u = 0.4$ ($|V_{\xi}(u = 0.4, \lambda)|$). For each curve we also show the maximum $|V|$ variation ($\Delta|V|$) and the σV error bars due to a 1% error in ρ_{eq} for ξ equal to $0°$ and $90°$.

The degeneracy that appears involves the combination of model parameters i, β and D, hereafter represented as (i, β, D). Although the curves shown in Fig. 5 represent just a few examples of the complete parameter space, they suffice to prove that observations performed uniquely in the first $|V|$ lobe and

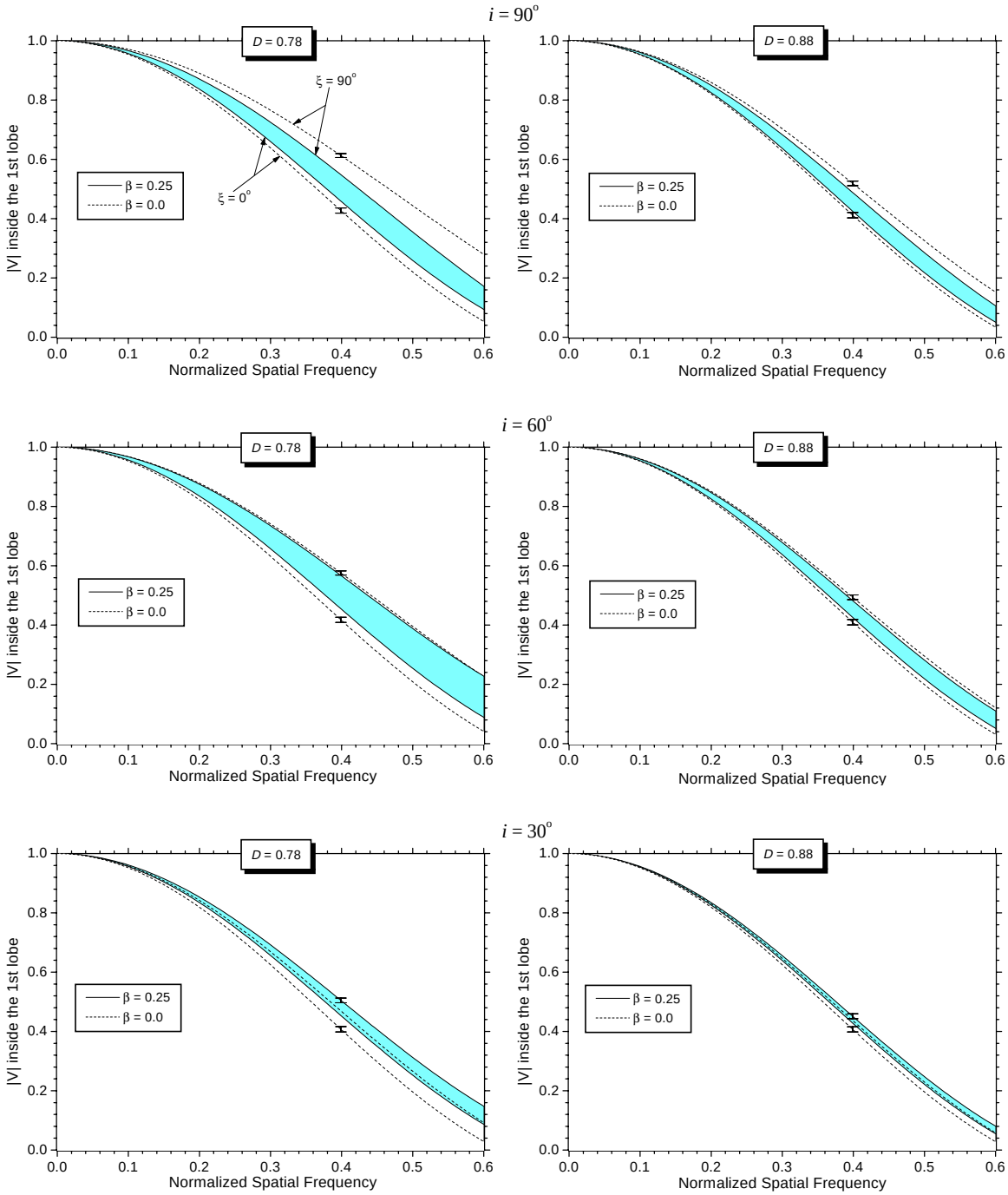

Fig. 4. Complex visibility amplitudes $|V|$ as a function of normalized spatial frequencies. Calculations were performed inside a narrow spectral band centered on the blue adjacent continuum corresponding to HeI6678 for models A and B (Table 1) at selected values of i and β. The curves of extreme ξ values (0° and 90°) are shown for $\beta = 0.25$ (solid curves filled in gray between them) and for $\beta = 0$ (dashed curves). Uncertainties in $|V|$ due to a 1% error in $\rho_{\rm eq}$ are represented as vertical error bars for the normalized spatial frequency 0.4. Only the error bars for the higher and lower $|V|$ curves are shown.

in single spectral bands present an important degeneracy in the values of i, β and D. As an illustration of this uniqueness problem we note the following two particular examples from Fig. 5 for which very similar $|V_\xi(u = 0.4, \lambda)|$ curves and values of $\Delta|V|$ are obtained by distinct parameter sets:

(*a*) the $|V_\xi(u = 0.4, \lambda)|$ curves for (30°, 0.0, 0.78) and for (90°, 0.25, 0.88) which present a $\Delta|V|$ of 0.062 and 0.063, respectively;

(*b*) the $|V_\xi(u = 0.4, \lambda)|$ curves for (30°, 0.25, 0.78) and for (60°, 0.25, 0.88) which present a $\Delta|V|$ of 0.051 and 0.057, respectively.

Additionally, the uniqueness problem is amplified if we consider the uncertainties σV due to $\sigma\rho_{\rm eq}$. In this case, the number of degenerated parameter combinations increases, particularly when only a narrow range of ξ values is covered by observations. However, we show hereafter that this degeneracy can be

greatly reduced by including information from the second $|V|$ lobe.

In order to explore the dependence of $|V|$ with ξ beyond the first lobe we chose two regions particularly sensitive to the model parameters (based in Fig. 3): the first minimum and the second lobe's maximum. They correspond, respectively, to the middle and bottom rows for a given i in Fig. 5. Note that if one can access several spatial frequency points until the second lobe the angular diameter is well constrained. Moreover, the uncertainties σV due to $\sigma\rho_{\rm eq}$ are negligible for the first minimum and second maximum.

Thus, by considering the $|V|$ curves at the first minimum and second lobe's maximum, it is clear that the ambiguities in the examples above are totally removed by the information coming from the second $|V|$ lobe. In the example (a) only the solution (90°, 0.25, 0.88) presents a second $|V|$ lobe's height strongly dependent on ξ, attaining values well above or below the theoretical one for uniform discs ($|V| = 0.132$). The remaining possible solution, (30°, 0.0, 0.78), presents a completely distinct behavior, with a roughly constant second lobe's height corresponding to a simple limb darkened star ($|V| \lesssim 0.132$). Analogously, observations in the second $|V|$ lobe can also disentangle the ambiguity in the example (b).

Even if the uncertainties σV are considered, information from the second $|V|$ lobe suffices to remove the ambiguities between the four parameter combinations from the examples (a) and (b) together. In fact, for these examples the second maxima alone suffice to disentangle the ambiguities, provided that we observe over a large ($\simeq$180°) range of ξ.

From these and other examples that can be found in Fig. 5 it is clear that information coming from the first and second $|V|$ lobes are complementary and that their combined use greatly reduces the degeneracy in the relevant model parameter determination. Note that precise observations in the second lobe require long integration times in order to compensate the low fringe contrast. This is because the signal to noise ratio varies as $N_{\rm ph}V^2$ (where $N_{\rm ph}$ is the number of photons). However, this should not be a major difficulty for the forthcoming interferometers, such as the Very Large Telescope Interferometer (VLTI), since they have large light collecting surfaces that will reduce the observation time.

However, the second $|V|$ lobe can be attained only for a few stars and, generally, additional theoretical and observational information should be used to reduce the degeneracy among different solutions. In the following we show that OLBI observations at different wavelengths are particularly suited for the study of gravity darkened stars even if we can observe only in the first $|V|$ lobe.

3.2. Multi wavelength OLBI in the first $|V|$ lobe

The stellar surface distribution of effective temperatures and gravities induced by rapid rotation results in a wavelength dependent sky-projected brightness distribution so that interferometric observations at distinct wavelengths can increase significantly the amount of information obtained about the star. This is shown by our calculations which were carried out on three distinct narrow spectral bands centered in continuum regions close to the lines SiIII4575 (blue), HeI6678 (red) and HeI10830 (near infrared). Figure 6 (top rows) shows the complex visibility amplitudes $|V_\xi(u = 0.4, \lambda)|$ versus ξ for different combinations of i, β and D, for these three continuum spectral bands. The σV error bars due to a 1% error in $\rho_{\rm eq}$ for ξ equal to 0° and 90° corresponding to the red spectral band are shown as well. The error bars for the blue and near infrared curves are not shown since they have roughly the same size as the plotted ones.

As expected, for a given spectral band the curves of $|V|$ versus ξ in Fig. 6 present the same kind of degeneracy as found in Fig. 5. However, by combining the information from the distinct spectral bands in Fig. 6 the degeneracy can be reduced even if we are only dealing with spatial frequencies inside the first lobe. This is visualized in the bottom rows of Fig. 6 (for fixed i) where we plot the differences between the visibility curves $\Delta|V_{\lambda_i,\lambda_j}| \left(\equiv |V_\xi(u = 0.4, \lambda_i)| - |V_\xi(u = 0.4, \lambda_j)|\right)$ for each pair of spectral regions (λ_i and λ_j).

Consider the example (a) in Sect. 3.1.2. The differences $\Delta|V_{\lambda_i,\lambda_j}|$ are less dependent on ξ for (30°, 0.0, 0.78) than for (90°, 0.25, 0.88). In example (b) the differences $\Delta|V_{\lambda_i,\lambda_j}|$ are both stronger and less dependent on ξ for (30°, 0.25, 0.78) than for (60°, 0.25, 0.88).

However, note that, even when $\beta = 0$, the $|V|$ curves are also dependent on the spectral band due to geometrical deformation and limb darkening. Consequently, the OLBI data at different spectral bands should present high signal to noise ratios for an effective decrease of the uniqueness problem. For the curves in Fig. 6, wavelength-relative error bars better than 1% would be required to resolve the ambiguities. These small error bars can in fact be obtained by the use of the differences in the $|V|$ because there will be a cancellation effect over all uncertainties that act in the same manner on the distinct $|V|$ curves. Only the residual uncertainties corresponding to non-correlated errors at each wavelength will remain in this differential technique.

This can be seen in the bottom rows of Fig. 6 where the maximum residual uncertainty due to a 1% error in $\rho_{\rm eq}$ is also plotted. Since $\rho_{\rm eq}$ is a scaling factor for all three $|V|$ curves, only small uncertainties in $\Delta|V_{\lambda_i,\lambda_j}|$ due to $\sigma\rho_{\rm eq}$ (less than 0.02%) remain after the differences are calculated. It is thus clear that differential visibilities $\Delta|V_{\lambda_i,\lambda_j}|$ with associated $\sigma\rho_{\rm eq}$ errors allow us to resolve the uniqueness problem, which is not the case if only absolute visibilities are considered. Practically, the benefits of this differential technique can be obtained by accessing several simultaneous spectral channels on a single baseline interferometer plus Earth-rotation synthesis or on a multi aperture interferometric array.

The differences $\Delta|V_{\lambda_i,\lambda_j}|$ can be further increased (in modulus) by many ways such as observing in more spaced wavelengths, higher spatial frequencies, or by choosing a spectral range that optimizes the differences for a given stellar spectral type and expected range of D and β.

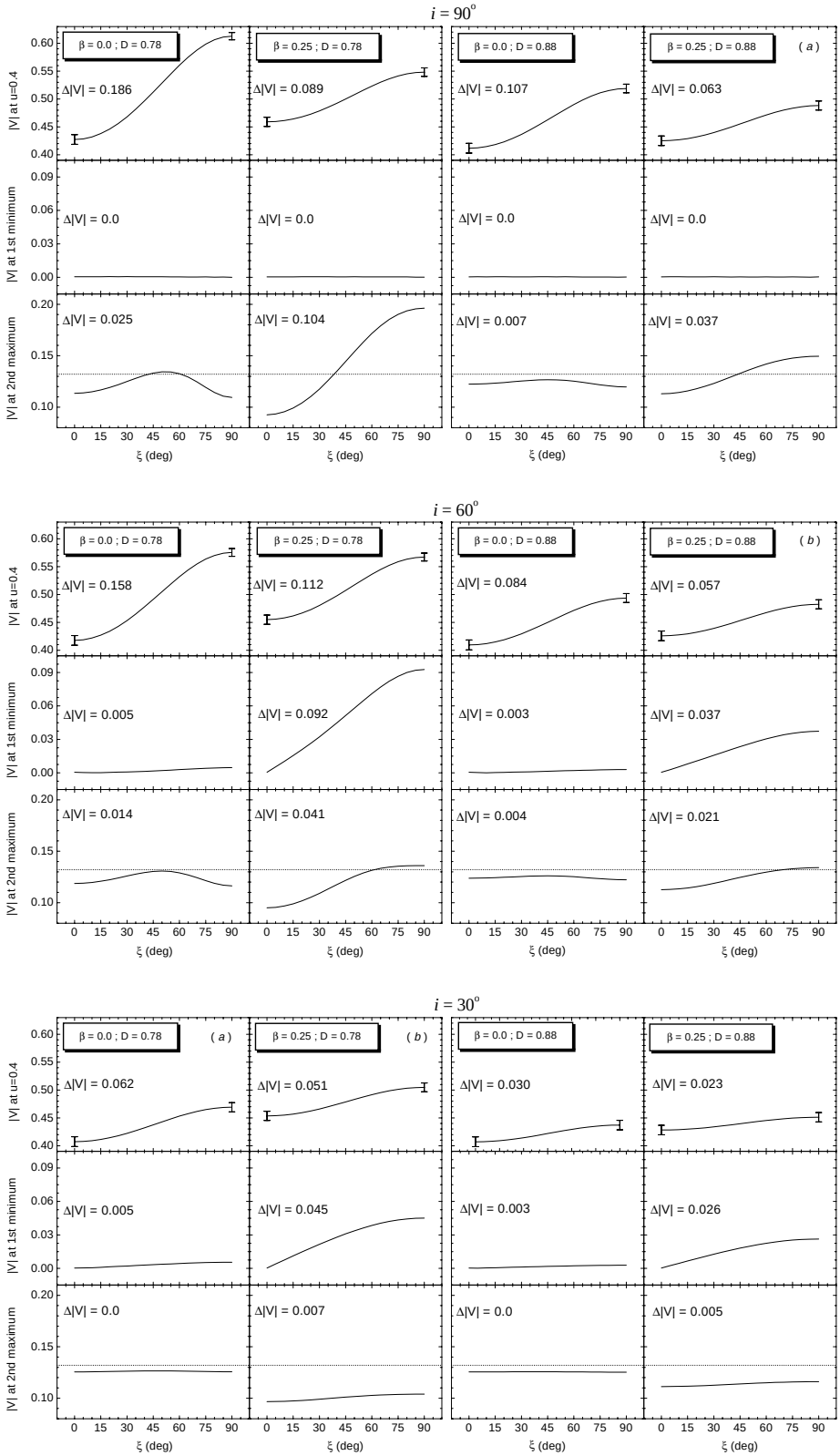

Fig. 5. Complex visibility amplitudes $|V|$ versus ξ for three particular regions: the normalized spatial frequency $u = 0.4$ (*top rows*), the first minimum (*medium rows*) and the second lobe's maximum (*bottom rows*). Calculations were performed inside a narrow spectral band centered on the blue adjacent continuum corresponding to HeI6678 for models A and B (Table 1) at selected values of i and β. For each curve, the maximum variation in $|V|$ (denoted by $\Delta|V|$) is indicated. The dotted lines on each second $|V|$ maximum curve indicate the theoretical value for uniform discs, $|V| = 0.132$; simple limb darkened spherical stars present second $|V|$ maxima slightly below this value. The error bars $\sigma|V|$ for the $|V_\xi(u = 0.4, \lambda)|$ curves correspond to a 1% error in $\rho_{\rm eq}$. These graphics show that the combined information from the first and second $|V|$ lobes reduce the ambiguities in the determination of the model parameters even when the uncertainties $\sigma|V|$ are considered. The parameter combinations *a* and *b* are examples of this statement.

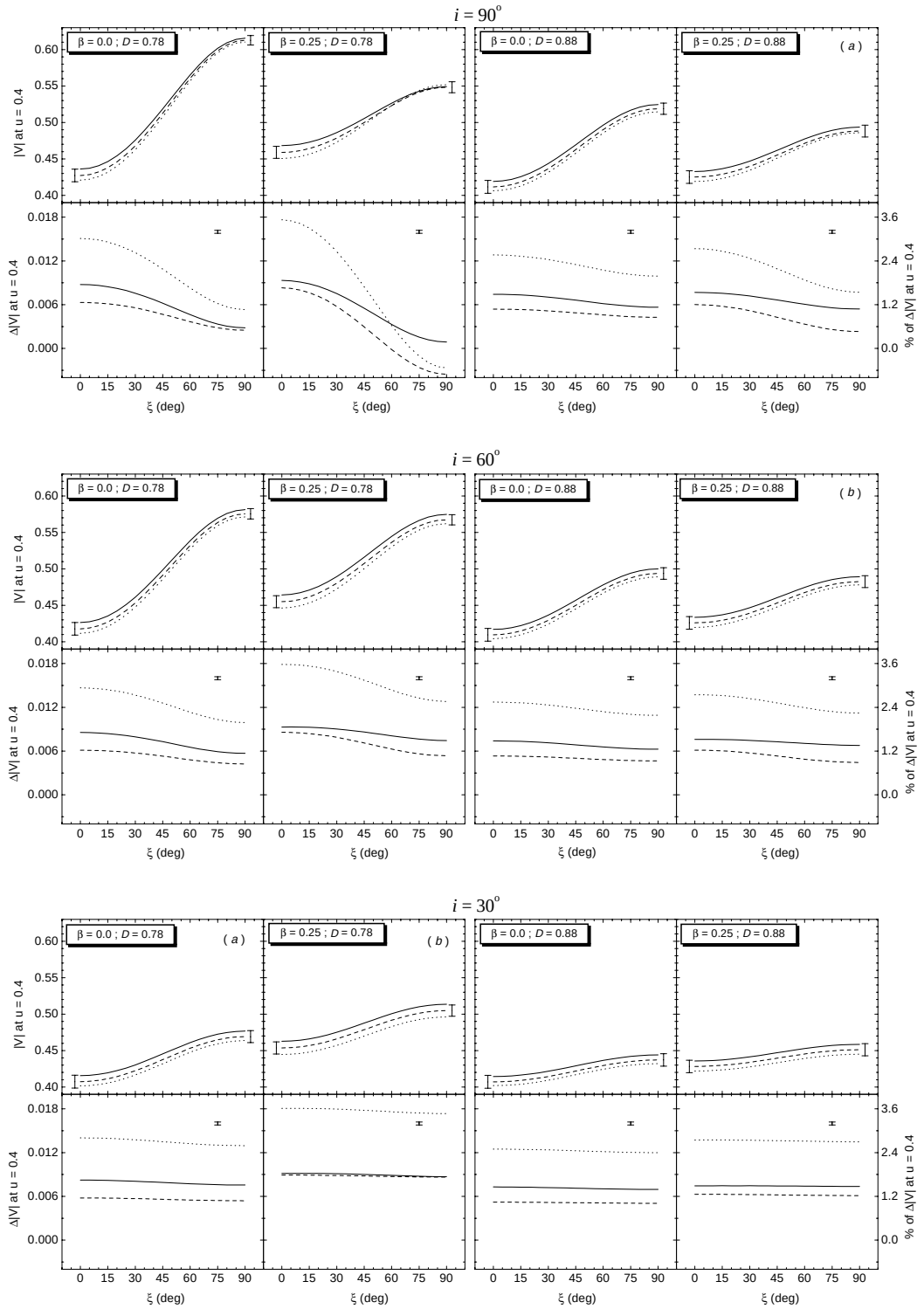

Fig. 6. (*Top rows*) Complex visibility amplitudes $|V_\xi(u = 0.4, \lambda)|$ versus ξ for the normalized spatial frequency $u = 0.4$. Calculations were performed for models A and B (Table 1) and different combinations of i and β (same values from Fig. 5). Three different spectral bands were adopted: λ_1 – red adjacent continuum corresponding to SiIII4575 (solid lines), λ_2 – blue adjacent continuum corresponding to HeI6678 (dashed lines) and λ_3 – blue adjacent continuum corresponding to HeI10830 (dotted lines). The σV error bars due to a 1% error in $\rho_{\rm eq}$ for ξ equal to 0° and 90° corresponding to the red spectral band are shown as well; they have been slightly displaced for better visualization. (*Bottom rows*) Differences $\Delta|V_{\lambda_i,\lambda_j}| \left(\equiv |V_\xi(u = 0.4, \lambda_i)| - |V_\xi(u = 0.4, \lambda_j)| \right)$ between the $|V|$ curves for each pair of spectral band. The curves correspond to $\Delta|V_{\lambda_1,\lambda_2}|$ (solid lines), $\Delta|V_{\lambda_2,\lambda_3}|$ (dashed lines) and $\Delta|V_{\lambda_1,\lambda_3}|$ (dotted lines). The percentage scale in the right axis represent 100% $\Delta|V_{\lambda_i,\lambda_j}|\ |\overline{V}|^{-1}$, where $|\overline{V}|$ is the mean of the visibility values; since for $u = 0.4$ $|\overline{V}|$ is always close to 0.5 this value was adopted for all curves. These graphics show that the uniqueness problem can be reduced by OLBI data obtained at distinct wavelengths even if only the first $|V|$ lobe is accessible. The error bars correspond to the maximum residual uncertainty due to $\sigma\rho_{\rm eq}$ after calculations of the differences $\Delta|V_{\lambda_i,\lambda_j}|$. The cases *a* and *b* are examples where data from distinct spectral bands remove the ambiguities from single spectral band observations.

3.2.1. Observations in absorption lines

For interferometers equipped with spectrographs another possibility to increase $\left|\Delta|V_{\lambda_i,\lambda_j}|\right|$ is to observe inside spectral lines. As an illustration we chose two photospheric absorption lines (SiIII4575 and HeII5412) presenting different behaviors with varying gravities (g) and effective temperatures ($T_{\rm eff}$). Figure 7 shows the local line profiles at selected g and $T_{\rm eff}$ covering some values that are expected to be found locally on the photosphere of main sequence rapidly rotating hot stars. The local profiles for HeI6678, which are less dependent on g and $T_{\rm eff}$, are also shown for comparison. While the HeI6678 line depends weakly on g and $T_{\rm eff}$, the HeII5412 and SiIII4575 depend strongly and inversely on these parameters. Consequently, the observed HeII line will be mainly formed close to the poles while the observed SiIII line will be mainly formed around the equator.

The opposed behavior of the HeII and SiIII lines with g and $T_{\rm eff}$ increases their spectral relative interferometric signatures due to fast rotation. This is seen in Fig. 8 where the top panel shows $|V|$ in a narrow spatial frequency region around $u = 0.4$, calculated inside four narrow spectral bands corresponding to the SiIII4575 and HeII5412 lines and part of their adjacent continua. The spectral band widths adopted here are a few angstroms wide and calculations were carried for model A seen pole on and $\beta = 0.25$. The $|V|$ curve obtained from the immediate continuum of SiIII4575 is slightly above the $|V|$ curve associated with the continuum of HeII5412 due to rapid rotation and limb darkening effects. Note that this behavior is identical to that of Fig. 6.

The intensity map $I_\lambda(y, z)$ corresponding to the spectral band centered in the SiIII4575 line presents a higher effective limb darkening compared to $I_\lambda(y, z)$ obtained for the adjacent continuum. On the other hand, the intensity map $I_\lambda(y, z)$ corresponding to the HeII5412 line presents a less important limb darkening compared to the adjacent continuum. As a result, the corresponding $|V|$ curves are displaced in opposite directions, amplifying appreciably the differences between them (top and bottom panels).

Since the continua were chosen close to the photospheric lines the discrepancy between the two curves in the bottom panel of Fig. 8 is only due to the particular absorption line dependencies on the rapid rotation effects. Finally, the bottom panel also shows how this discrepancy increase with the spatial frequency inside the first $|V|$ lobe.

Consequently, when the interferometer offers a spectral resolution allowing measurements inside individual spectral lines, it is possible to study gravity darkened rapidly rotating stars, inside the first $|V|$ lobe, even with a relatively narrow wavelength coverage.

It should be mentioned that, for high $V_{\rm eq} \sin i$ (compared to the intrinsic line width), these line effects are spread in wavelength due to rotation broadening and the relatively stronger contribution of the continuum diminishes the line effects on the interferometric observables. For small stellar inclinations, line contributions are concentrated in a narrower spectral region and the relative contribution of the continuum is smaller. The simultaneous use of many lines with similar behaviors can increase the signal to noise ratio in real observations. For example one could add data on the remaining two lines of the SiIII triplet (centered at 4552 and 4567 Å) that present a similar behavior to SiIII4575.

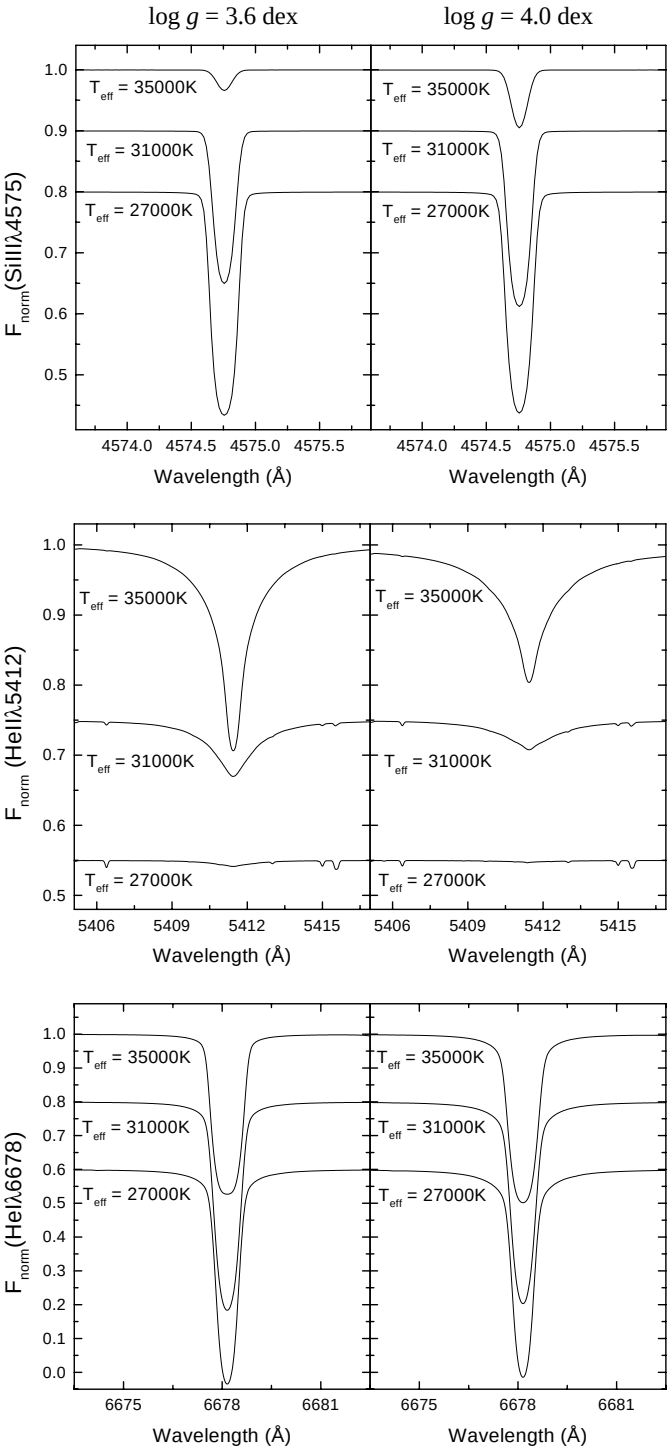

Fig. 7. Normalized flux $F_{\rm norm}$ obtained from the adopted plane parallel model atmospheres (Sect. 2.3) for SiIII4575, HeII5412 and HeI6678. Calculations were performed for selected values of $\log g$ and $T_{\rm eff}$ that are expected to be found locally on the photosphere of main sequence rapidly rotating hot stars. Note the distinct line profile behaviors presented by these three absorption lines. Curves were arbitrarily displaced and weak line blends were removed for better visualization.

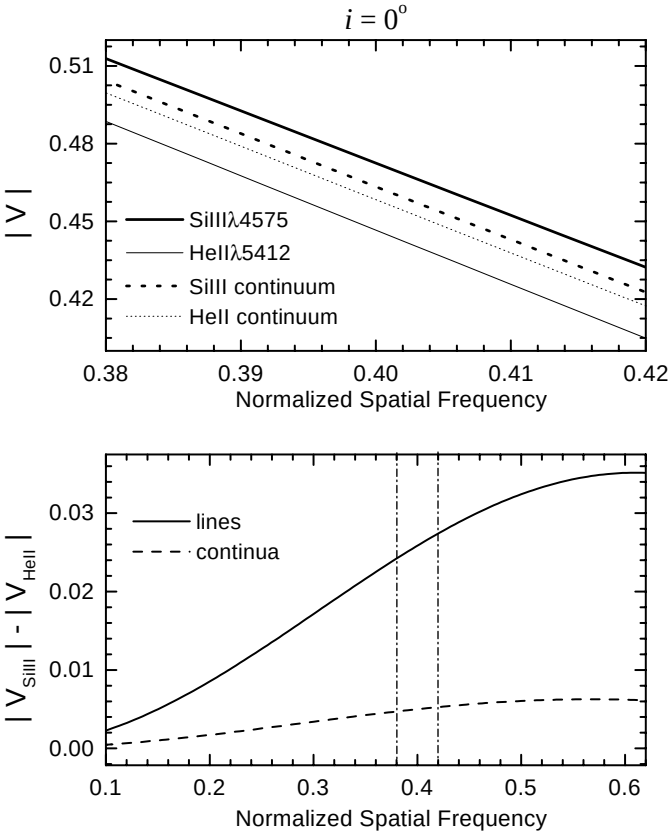

Fig. 8. (*Top panel*) Complex visibility amplitude $|V|$ over a narrow spatial frequency region around $u = 0.4$ for model A (Table 1) seen pole on and $\beta = 0.25$. Thin dotted and solid curves represent, respectively, $|V|$ in the red adjacent continuum relative to HeII5412 and to the HeII line itself. Analogously, thick dotted and solid curves represent the red adjacent continuum relative to SiIII4575 and to the SiIII line itself. The two curves corresponding to the photospheric lines are much more separated than the two curves corresponding to their immediate continua. (*Bottom panel*) $\Delta|V_{\lambda_i,\lambda_j}|$ versus the normalized spatial frequency covering a large region of the first $|V|$ lobe. The solid curve represents differences between the $|V|$ curves for spectral bands centered in the SiIII and HeII absorption lines while the dashed one represents differences between the $|V|$ curves for spectral bands centered in the adjacent continua of those absorption lines. The dot-dashed vertical limits indicate the spatial frequency domain corresponding to the top panel.

4. Conclusions

The interferometry-oriented model described in this work was used to evaluate the rapid rotation signatures on interferometric observables and to investigate how the degeneracy of solutions problem can be overcome.

Observations performed only in the first $|V|$ lobe and in a single spectral band present an important degeneracy in the values of i, D and β. In general this degeneracy leads to an ambiguity between highly deformed low i stars and lowly deformed high i stars. An additional effect is a partial cancellation of the geometrical deformation due to gravity darkening. This cancellation effect was initially mentioned by Johnston & Wareing (1970). It was confirmed and quantitatively estimated here also for a larger parameter space domain.

It was shown that if observations are not carried out between the extreme values of ξ (0° and 90°) there will be a degeneracy associated with the value of ξ and consequently with the projected stellar deformation signature. Practically, this degeneracy can be removed by performing the observations at several baseline orientations in a way that one covers a large range of ξ values. We also show that the information from the second $|V|$ lobe, when accessible, suffices to disentangle the ambiguities between relevant parameter combinations.

Further, it turns out that the access to several simultaneous spectral channels on a single baseline interferometer and/or on a multi-aperture plus Earth-rotation synthesis array brings stronger constraints through continuously sampled and/or multi-direction spatial resolution visibility data to resolve the uniqueness problem, as discussed in Sect. 3. For such types of observations the uniqueness of solutions can be obtained even if we can observe the star only in the first $|V|$ lobe.

The GI2T interferometer (Mourard et al. 2000) illustrates the case of spectrally resolved interferometry where its lowest spectral resolution of ∼1200 provides several hundred simultaneous visibility samples at different spatial frequencies as a function of the wavelength which can additionally benefit from a 40 degree maximum Earth-rotation synthesis. The VLTI (Glindemann et al. 2000) with its 21 future baseline orientations (7 telescopes) can certainly solve the uniqueness problem for rapid rotators, opening the possibility for a survey of rapid rotation effects across the H-R diagram.

Our calculations showed that interferometric observations of rapid rotators require high fringe contrast sensitivity ($|V| \simeq 0.1$) with small error bars ($\lesssim$1%). Such performances are already attained by the present generation of stellar interferometers like the VLTI, PTI (Colavita et al. 1999) or IOTA (Hofmann et al. 2002). This is specially true in the case of fiber-linked mono-mode stellar interferometers such as FLUOR (Coudé du Foresto et al. 1997). For multi-mode interferometers like the GI2T and the VLTI/AMBER (Petrov et al. 2000) more subtle effects such as differential stellar rotation and/or non-radial pulsations (Jankov et al. 2001) could be addressed by interferometric diagnosis.

Acknowledgements. A.D.S. acknowledges CAPES – Brazil (contract BEX 1661/98-1) and the GI2T team for financial support. We thank Dr. R.H.D. Townsend for helpful comments about the BRUCE code. This paper as largely benefitted from critical suggestions of Dr. A. Reiners. We also acknowledge Drs. J. F. Pacheco, D. Bonneau, P. Stee, D. Mourard and O. Chesneau for critical discussions.

References

Born, M., & Wolf, E. 1980, Principle of Optics (Pergamon Press, Oxford)
Bracewell, R. N. 1956, Aust. J. Phys., 9, 198
Claret, A. 1998, A&A, 131, 395
Claret, A. 2000, A&A, 359, 289
Colavita, M. M., et al. 1999, ApJ, 510, 505
Collins, G. W., II 1963, ApJ, 138, 1134
Collins, G. W., II 1965, ApJ, 142, 265
Collins, G. W., II, & Harrington, J. P. 1966, ApJ, 146, 152
Connon Smith, R., & Worley, R. 1974, MNRAS, 167, 199

Coudé Du Foresto, V., Ridgway, S., & Mariotti, J.-M. 1997, A&AS, 121, 379
Glindemann, A., et al. 2000, SPIE Proc., 4006, 2
Pérez Hernández, F., Claret, A., Hernández, M. M., & Michel, E. 1999, A&A, 346, 586
Hanbury Brown, R. 1974, in The Intensity Interferometer (ed. Taylor & Francis LTD, London), 151
Hofmann, K.-H., et al. 2002, New Astron., 7, 9
Hubeny, I. 1988, Comp. Phys. Comm., 52, 103
Hubeny, I., & Lanz, T. 1995, ApJ, 439, 875
Jankov, S., Vakili, F., Domiciano de Souza, Jr., A., & Janot-Pacheco, E. 2001, A&A, 377, 721
Johnston, I. D., & Wareing, N. C. 1970, MNRAS, 147, 47
Kopal, Z. 1987, Astrophys. Space Sci., 133, 157
Kurtz, D. W. 1985, MNRAS, 213, 773
Lucy, L. B. 1967, Z. Astrophys., 65, 89
Mourard, D., et al. 2000, SPIE Proc., 4006, 434
Petrov, R. G., et al. 2000, SPIE Proc., 4006, 68
Perryman, M. A. C., et al. 1997, A&A, 323, L49
Reiners, A., & Schmitt, J. H. M. M. 2002, A&A, 384, 155
Townsend, R. H. D. 1997, MNRAS, 284, 839
Vakili, F., Mourard, D., Bonneau, D., Morand, F., & Stee, P. 1997, A&A, 323, 183
van Belle, G. T., Ciardi, D. R., Thompson, R. R., Akeson, R. L., & Lada, E. A. 2001, ApJ, 559, 1155
von Zeipel, H. 1924, MNRAS, 84, 665